Target Deconvolution of a Multikinase Inhibitor with Antimetastatic Properties Identifies TAOK3 as a Key Contributor to a Cancer Stem Cell–Like Phenotype

Yansong Bian[1], Yaroslav Teper[2], Lesley A. Mathews Griner[3], Taylor J. Aiken[2,4], Vivek Shukla[2], Rajarshi Guha[3], Paul Shinn[3], Hong-Wu Xin[2], Holger Pflicke[2], Astin S. Powers[5], Dandan Li[1], Jian-kang Jiang[3], Paresma Patel[3], Steven A. Rogers[6], Jeffrey Aubé[6], Marc Ferrer[3], Craig J. Thomas[3], and Udo Rudloff[1]

Abstract

Pancreatic cancer remains an incurable condition. Its progression is driven, in part, by subsets of cancer cells that evade the cytotoxic effects of conventional chemotherapies. These cells are often low-cycling, multidrug resistant, and adopt a stem cell–like phenotype consistent with the concept of cancer stem cells (CSC). To identify drugs impacting on tumor-promoting CSCs, we performed a differential high-throughput drug screen in pancreatic cancer cells cultured in traditional (2D) monolayers versus three-dimensional (3D) spheroids which replicate key elements of the CSC model. Among the agents capable of killing cells cultured in both formats was a 1H-benzo[d]imidazol-2-amine–based inhibitor of IL2-inducible T-cell kinase (ITK; NCGC00188382, inhibitor #1) that effectively mediated growth inhibition and induction of apoptosis *in vitro*, and suppressed cancer progression and metastasis formation *in vivo*. An examination of this agent's polypharmacology via *in vitro* and *in situ* phosphoproteomic profiling demonstrated an activity profile enriched for mediators involved in DNA damage repair. Included was a strong inhibitory potential versus the thousand-and-one amino acid kinase 3 (TAOK3), CDK7, and aurora B kinases. We found that cells grown under CSC-enriching spheroid conditions are selectively dependent on TAOK3 signaling. Loss of TAOK3 decreases colony formation, expression of stem cell markers, and sensitizes spheroids to the genotoxic effect of gemcitabine, whereas overexpression of TAOK3 increases stem cell traits including tumor initiation and metastasis formation. By inactivating multiple components of the cell-cycle machinery in concert with the downregulation of key CSC signatures, inhibitor #1 defines a distinctive strategy for targeting pancreatic cancer cell populations.

Introduction

Pancreatic cancer currently ranks fourth among all cancer-related deaths in the United States and is estimated to rank second by the year 2030 (1, 2). The 5-year survival rate of the disease is approximately 5% and has not significantly changed over the last three decades. Early systemic spread and insurmountable drug resistance are the primary drivers of these dismal outcomes (3). Patients who undergo surgical resection inevitably recur with metastases to the liver, lungs, and peritoneum due to preexisting micrometastases which evade eradication by adjuvant systemic chemotherapy. Current systemic chemotherapy regimens extend median overall survival by 4.3 and 1.8 months relative to single-agent gemcitabine therapy (4, 5). These incremental gains underscore the dire need for alternate approaches to treating this disease.

Improved insight into tumoral heterogeneity has supported the concept of progenitor-like cancer cells often referred to as cancer stem cells (CSC). These populations of less differentiated cells maintain the ability to self-renew and are drivers for therapeutic resistance and rapid recurrence (6, 7). CSCs are postulated to reside in specific niches characterized by low oxygen tension, limited nutrient supply, and high redox load (8, 9). CSCs are highly protective of their genome via upregulation of a variety of DNA damage repair (DDR) mechanisms and fail to undergo

[1]Rare Tumor Initiative, Pediatric Oncology Branch, Center for Cancer Research, National Cancer Institute, Bethesda, Maryland. [2]Thoracic and GI Oncology Branch, Center for Cancer Research, National Cancer Institute, Bethesda, Maryland. [3]Division of Pre-Clinical Innovation, National Center for Advancing Translational Sciences, National Institutes of Health, Rockville, Maryland. [4]Department of Surgery, University of Wisconsin, Madison, Wisconsin. [5]Laboratory of Pathology, Center for Cancer Research, National Cancer Institute, Bethesda, Maryland. [6]Division of Chemical Biology and Medicinal Chemistry, UNC Eshelman School of Pharmacy, Chapel Hill, North Carolina.

Note: Supplementary data for this article are available at Molecular Cancer Therapeutics Online (http://mct.aacrjournals.org/).

Y. Bian, Y. Teper, and L.A. Mathews Griner contributed equally to this article.

Corresponding Authors: Udo Rudloff, Center for Cancer Research, National Cancer Institute, Bethesda, MD 20892. Phone: 240-760-6238; Fax: 301-451-6933; E-mail: rudloffu@mail.nih.gov; and Craig J. Thomas, Division of Preclinical Innovation, NIH Chemical Genomics Center, National Center for Advancing Translational, Sciences (NCATS), 9800 Medical Center Drive, Rockville, MD 20850. Phone: 301-217-5733; E-mail: craigt@mail.nih.gov

Mol Cancer Ther 2019;18:2097–110

doi: 10.1158/1535-7163.MCT-18-1011

programmed cell death or enter senescence upon treatment with genotoxic agents (7, 10). These cells exaggerate key DDR mechanisms including accelerated homologous recombination (HR), nonhomologous end joining, ATR-, and Ataxia-telangiectasia mutated (ATM)–mediated cell-cycle checkpoint regulation, or metabolic reprogramming (11–16). Selectively targeting CSC, alone or in combination with cytotoxic agents, as a means to produce durable remissions is an appealing concept.

Recently, both homogenous spheroid models and organoid models have been advanced into drug screening studies in hopes of better targeting these CSC subpopulations to provide more appropriate leads for clinical translation (17, 18). In drug screening models, only cellular spheroids represent reliable high-throughput screening (HTS)–compatible *in vitro* models that consistently demonstrate an upregulation of known CSC markers and capture tumoral cell heterogeneity and microenvironmental factors (6, 19–23). For most next-generation therapies, system-guided target deconvolution of HTS-derived hits is required to enable a complete mechanism-to-phenotype understanding (24, 25). Many effective oncology drugs originally discovered for one target were ultimately found to harbor a distinct polypharmacology profile essential to mediate antitumor activity (26, 27). Understanding the drivers of drug actions can improve the probability of identifying synergistic and additive drug combinations and further the chances of finding effective drug/drug combinations capable to targeting otherwise drug-resistant cancer cell populations (25).

Here, we describe the identification of a previously reported small-molecule inhibitor of the IL2-inducible T-cell kinase (ITK; NCGC00188382, inhibitor #1) as an agent with pan-killing of the spheroid harboring CSC features and 2D monolayer phenotype of pancreatic cancer cells (28). The compound effectively induces apoptosis in spheroid cultures, inhibits invasion, and suppresses cancer stemness traits including tumor initiation and metastasis formation. We identified a distinct polypharmacology profile for this agent which includes key regulators of DDR pathways including the MAPKK kinase TAOK3 as a novel key driver of the resultant anti-CSC phenotype. Combinatorial matrix screening identified selected drug combinations which further enhanced this agent's activity. The outcomes of these studies validate DDR as an Achilles heel of CSCs.

Materials and Methods

Cell lines and materials

The origin of the human ovarian carcinoma cell line A2780, the kidney carcinoma cell line SN12C, and 24 human pancreatic cancer cell lines derived from primary and secondary sites used in this study is listed in Supplementary Table S1. Cells were maintained according to instructions from supplier or in RPMI 1640 medium with 10% (v/v) FBS and incubated at 37°C in a 5.0% CO2 atmosphere. In accordance with AACR practices, cells were authenticated by SNP genotyping using Illumina MiSeq sequencing. Anti-CD133-FITC (orb378636) and IgG_2 isotype control-FITC antibodies (orb343834) were purchased from Biorbyt, anti–phospho-p38 MAPK(Thr180/Tyr182) (Cat. #9215), phospho-MKK3 (Ser189)/MKK6(Ser206) (Cat. #12280) from Cell Signaling Technology, anti-phospho histone H3 (S10) (ab5176) and anti-histone H3 (ab1791) from AbCam, EphB2(H-80) antibody (sc-28980), p-Tyr(PY20) (sc-508) antibody, and protein A/G PLUS-Agarose (sc-2003) from Santa Cruz Technologies. Actinomycin D (S4964), alvespimycin (17-DMAG, S1142), AUY-922 (S1069), carfilzomib (S2853), and AZD1172 (S7263) were purchased from Selleck Chem, Inc. A detailed synthesis scheme of inhibitor #1 (S, E)-N-(5-(((3,3-dimethylbutan-2-yl) amino) methyl)-1-(2-hydroxy-2-methylpropyl)-1,3-dihydro-2H-benzo[d]imidazol-2-ylidene)-5-(1H-pyrazol-4-yl) thiophene-2-carboxamide (NCGC00188382) is shown in Supplementary Fig. S1.

Spheroid culture conditions

Multicellular tumor spheroids from PANC1, KLM-1, L3.6pl, MiaPaCa-2, and the primary low-passage tissue culture line SB.06 derived from the primary tumor of a pancreatic cancer patient were created as previously described (29). In brief, 30,000 to 100,000 cells grown under conventional monolayer 2D conditions were seeded in 15 to 20 mL stem cell media (SCM) onto nonadherent T75 flasks coated with hydrogel (Corning Life Sciences). Note that 500 mL SCM contained 1:1 DMEM: F12 media (Cat. #11320-033, Life Technologies), 5 mL 100x ITS media supplement (Cat. #13146, Sigma), 2 g BSA (0.40%; Cat. #A2153, Sigma), 1% KnockOut Serum Replacement (Cat. #10828028), 20 ng/mL human EGF (Cat. #E9644, Sigma), and 10 ng/mL human FGF (Cat. #F0291, Sigma). Spheroids were grown at 37°C for 14 days. Spheroids were harvested and mechanically dissociated via gentle up-and-down pipetting for 2 to 3 minutes using a motorized Levo Plus Pipette Filler (Cat. #74020002; Scilogex) set on low speed. Single-cell suspensions were confirmed under the microscope and counted prior to re-seeding in SCM. Spheres were allowed to reform for 48 to 72 hours prior to drug testing or transfection with siRNA (abbreviated spheroid protocol; refs. 29, 30).

1536-well quantitative high-throughput screen of PANC1 spheroids

Design of the quantitative HTS drug screen in multicellular PANC1 spheres has previously been described (30). Hits were selected by a combination of parameters including percent viability at the compound dose that produced maximum cell killing and curve response class classification as previously described (30).

KiNativ kinome screening of PANC1 cells

In situ analysis of PANC1 cells cultured in monolayer or spheroid format treated with 100 and 500 nmol/L of inhibitor #1 for 24 hours was performed as previously described (31).

Drug-response profiles

The effects of inhibitor #1, other small-molecule inhibitors, and chemotherapy agent actinomycin D on proliferation were tested by seeding 5,000 cells per well in 96-well plates and incubating them for 24 hours before addition of increasing concentrations of drug to each well in three replicates with DMSO as negative control. For 3D spheroid drug-response testing, spheroids were dissociated with trypsin, counted, and seeded in SCM on low-attachment plates. After start of spheroids formation (48–72 hours after seeding), drug was added. Plates were read after 72 hours following addition of Promega Cell Titer Glo assay reagent (Promega) in a GloMax 96 Microplate Luminometer (Promega), and data analyzed using SoftMax version 5 and GraphPad Prism version.

HTS combinatorial matrix screening of #1 in PANC1 spheroids

The high-throughput combination screening platform on which a wide range of dosages for pairs of small-molecule inhibitors was conducted was previously described (25).

Fluorescence-activated cell sorting and Annexin V/PI staining

The Alexa Fluor 488 Annexin V/Dead Cell Apoptosis Kit from Life Technologies was followed. Note that 5×10^4 cells were seeded onto 6-well dishes or 3×10^5 cells per flask into T-25 flasks and incubated at 37°C for 48 to 72 hours prior to addition of inhibitor #1. Induction of apoptosis was quantified by binding of Annexin V in treated versus DMSO-control cells. For CD133 cell surface cell sorting, both PANC1 spheres and adherent monolayer cells were harvested as above, washed, stained including isotype controls, and sorted as previously described (20, 29).

Migration and invasion assay

Matrigel-coated 24-well inserts (8-μm pore size) and non-coated control inserts purchased from BD Biosciences Clontech were used. Both, 2.5×10^4 dissociated PANC1 spheres and 2D monolayer cells were used as previously described. After 18 hours, cells on the inserts were stained with the Diff Quick staining kit (Dade Bearing, Inc.).

PANC1*luc2* and KLM-1 *TAOK3*^{OE} orthotopic pancreatic cancer metastases model

All animal procedures were approved by the National Cancer Institute Animal Care and Use Committee of NIH. Sixty thousand PANC1 cells stably transfected with pGL4.10[luc2] luciferase reporter vector (Promega) were derived from PANC1 spheroids after gentle mechanical dissociation, counted, and transplanted via left subcostal incision, dissection of the distal pancreas, and injection into the tail of NOD-scid IL2Rgamma^{null} (NSG) immunodeficient mouse pancreata (mouse strain #005557, The Jackson Laboratory). Mice were administered either saline (vehicle) or 10 mg/kg of inhibitor #1 administered in polyethylenglycol (PEG)/H_2O = 70:30 via i.p. injection daily starting 28 days after transplantation and continuing until 10 weeks. Mice were then injected with 4.5 mg of luciferin i.p., sacrificed after 5 minutes, primary tumor, lungs, and liver procured and transferred to 6-well plates, and imaged for 5 minutes in Xenogen Bioluminescence instrument. Groups were compared with the Wilcoxon–Mann–Whitney test. Confidence intervals for the differences in the mean of uncorrected bioluminescence readings between two groups were computed by the bias-corrected and accelerated bootstrapping methods. P values were adjusted for multiple testing by complete resampling, $P < 0.05$ was considered significant. After imaging, all tissues were weighed and fixed in 4% paraformaldehyde. After hematoxylin and eosin (H&E) staining, metastatic deposits were manually counted under 25x magnification and compared with the Wilcoxon–Mann–Whitney test. For overexpression of TAOK3, 60,000 KLM-1 3D spheroids previously transduced with empty vector (TAOK3^{EV}) or TAOK3 (TAOK3^{OE}) were dissociated, counted, and injected into the tail of the pancreas of NSG mice. Mice of both groups were harvest at 12 weeks after implantation upon appearance of palpable abdominal masses and subjected to necropsy. Liver metastasis (the sum of the volumes of individual metastasis of examined cut liver surface, μm^2) was calculated as the sum of the volumes of the individual metastasis of 100 randomly selected high-power fields.

Subcutaneous murine xenograft experiments

PANC1*luc2* cells derived after mechanical dissociation of 3D spheroids were suspended in PBS at a concentration of 1×10^6 cells/100 μL and inoculated subcutaneously into flanks of 6- to 8-week-old NSG mice (8 mice per treatment group per experiment). Mice were monitored twice weekly. After approximately 28 days when tumors had reached a diameter of 0.5 to 0.7 cm, mice were given saline (vehicle), 1 mg/kg, or 10 mg/kg of inhibitor #1 administered in PEG/H_2O = 70:30 via i.p. injection daily. Tumor growth was monitored using Xenogen bioluminescence imaging twice weekly. Groups were compared with the Wilcoxon–Mann–Whitney test. Confidence intervals for the differences in the mean of uncorrected bioluminescence readings between two groups were computed by the bias-corrected and accelerated bootstrapping methods. P values were adjusted for multiple testing by complete resampling, and $P < 0.05$ was considered significant.

To assess tumor initiation, 1,000 SB.06 or PANC1 2D monolayer cells or cells derived after mechanical dissociation of 3D spheroids, resuspension in serum-free HBSS, and counting were s. c. injected into the flank of female athymic nude (nu/nu) mice (mouse strain #002019, The Jackson Laboratory). Tumor volume (mm^3) was calculated via as $(L \times W^2)/2$, with L = length (mm) and W = width (mm) during 2D caliper measurements. Similarly, fully developed KLM-1 spheroids (grown for >14 days in SCM) previously transduced with empty vector (TAOK3^{EV}) or TAOK3 (TAOK3^{OE}) were dissociated and counted. One thousand KLM-1 cells derived from dissociated KLM-1 spheroids were injected into female (nu/nu) mice, and tumor volume was recorded twice a week.

Cell proliferation and transient siRNA transfection

siRNAs targeting the 8 top hits of the KiNativ screen were purchased from Qiagen. Four siRNAs targeting, different regions of each gene were obtained. Either siRNAs with already validated target knockdown were tested or BLOCK-iT RNAi Designer (Invitrogen) or siRNA Target Finder (Ambion) software was used to design siRNAs for targets with nonvalidated knockdown efficacy. Cells were transfected with siRNA and Lipofectamine-2000 according to the manufacturer's instructions.

Reverse-phase protein microarrays

Reverse-phase protein microarray (RPMA) analysis of both PANC1 spheroids and 2D monolayer cells was performed as previously described (32). In brief, 2D monolayer cells and 3D spheroids grown in their respective media and conditions on T75 flask were treated with 500 nmol/L inhibitor #1 or DMSO control, harvested after 8 hours, and lysed in 2.5% solution of 2-mercaptoethanol in loading buffer/T-PER plus phosphatase and protease inhibitors (cOmplete Protease Inhibitor Cocktail Tablets, Sigma; Phosstop Phosphatase Inhibitor Cocktail, Roche Biochem). Samples were transferred on dry ice to Theranostics Health, LLC, for the reverse-phase protein array analysis according to proprietary protocols. In brief, samples were diluted to a final concentration of 0.5 mg/mL, and then 30 μL of each sample was spotted onto glass slides in a series of 6-fold dilutions. The slides were probed with a panel of previously validated 100 antibodies primarily directed against specific phosphorylated or cleaved proteins (32). Each slide included a Sypro Ruby protein blot stain (Invitrogen) to allow for normalization of all end point values, and each value

was normalized relative to the total protein intensity value for that sample derived from the Sypro Ruby–stained slide. Data were retrieved, averaged, and preprocessed by $\log_2$ transformation and z-score conversion to ensure data normality and linearity. Software R version 3.1.1 was used for heatmap generation, because comparisons were made between 2D and 3D cells only, and no FDR (q value) or P values were given.

Immunofluorescence

To enable accurate staining of 3D spheroid cells, a protocol of cytocentrifugation followed by fixation and staining was employed. Fully grown spheroid suspensions from T75 flasks were harvested, mechanically dissociated, and after counting approximately 50,000 cells, loaded onto a Rotofix 32A Cyto centrifuge (Hettich Lab Technology), and at 800 rpm transferred to glass slides and immediately fixed in methanol at room temperature for 2 minutes. 2D monolayer cells were subject to the same protocol prior to cytocentrifugation and transfer. Cells were permeabilized in 0.25% TritonX-100 and blocked with 5% normal goat serum in PBS at room temperature in a humidified chamber for 2 hours. Slides were incubated with rabbit monoclonal anti-human NOTCH1 (Cat. #4380, Cell Signaling Technology), cleaved NOTCH1 (Cat. #4147, Cell Signaling Technology), mouse monoclonal anti-human phospho-H2A.X (Cat. #05-636-AF555; Millipore Sigma) primary antibody, or rabbit IgG or mouse G3A1 IgG_1 isotype control overnight in 4°C. Alexa Fluor 488 goat anti-rabbit IgG (H + L; Cat. #A27034; ThermoFisher Scientific, Inc.) or Alexa Fluor 555 goat anti-mouse IgG (H + L; Cat. #A-21422; ThermoFisher Scientific) secondary antibody was then applied for 1 hour at room temperature. Slides were mounted with Vectashield/DAPI (Vector Laboratories). Images were captured using a Zeiss LSM 510 UV or Zeiss LSM 780 confocal microscope (Zeiss).

Immunohistochemical staining

Immunostaining was performed on formalin-fixed, paraffin-embedded tissue sections using a dual IHC staining method. After deparaffinization and hydration, heat-induced antigen retrieval was performed using high pH EDTA buffer (Cat. #61215, NDBbio, LLC). Endogenous peroxidases were quenched with 3% hydrogen peroxide solution. Primary antibody incubation was performed with cleaved NOTCH1 rabbit monoclonal antibody (clone D3B8, Cat. # 4147, Cell Signaling Technology, Inc.) for 80 minutes. A horseradish peroxidase–conjugated anti-rabbit secondary antibody was applied, and chromogenic signal was developed with DAB. Second antibody incubation was performed using rabbit monoclonal E-Cadherin antibody (clone EP700Y, Cat. # MA5-14458, ThermoFisher Scientific, Inc.) at a dilution of 1:200 for 32 minutes, and staining was developed with a red chromogen. Samples were counterstained with hematoxylin and dehydrated for permanent mounting.

Statistical analysis

Data were statistically analyzed using SPSS software version 16 (IBM). Continuous data, including gene expression values, immunofluorescence intensities, and tumor measurements, were compared using GraphPad Prism Student t test. Error bars indicate SEM unless otherwise indicated. Calculated P values were given by number of asterisk(s): *, $P < 0.05$; **, $P < 0.01$; and ***, $P < 0.001$.

Results

Pancreatic cancer spheroids possess CSC-like properties

We first validated that cultured pancreatic cancer cell spheroids forced into 3D architecture (Fig. 1A) adopt progenitor-like features using a multipronged approach. Gene transcripts of key stemness genes associated with stemness showed increased expression levels in pancreatic cancer cells grown as spheroids compared with 2D monolayer cells (Fig. 1B). Several of these signatures occurred as early as 24 hours following implementation of 3D culture methods (Supplementary Fig. S2). In line with low oxygen tension and nutrient deprivation in the center of 3D spheroids, phosphoproteomic examination of PANC1 spheroids showed relative increase in stress-related signaling [p90RSK3 (T356/S360), p38 MAPK (T180/Y182); Fig. 1C]. Activated NOTCH1 signaling as well as an increased fraction of $CD133^{+}$ cells was noted in spheroid cultures relative to monolayer cells (Fig. 1D and E). Spheroid cultures showed increased resistance to gemcitabine treatment as measured by the DNA damage marker γ-H2AX and caspase 3/7 activation (Fig. 1F). Upon injection into immunocompromised nu/nu mice, mice injected with spheroidal cultures demonstrated more tumors as well as tumors of greater size (Fig. 1G). These results suggest that pancreatic cancer cells grown as 3D spheroids are enriched with CSCs.

Comparative drug screening identifies candidate anti-CSC agents

To identify lead agents with enhanced anti-CSC activity, we screened PANC1 cells grown in spheroid and monolayer formats utilizing previously reported methods with a library of approximately 2,000 approved and investigational drugs (PubChem AID 1259363; Supplementary Table S2). Generally, a higher dose was required to achieve maximum cell killing in the spheroid cultures. Among the agents to display a nearly equipotent effect in spheroid and monolayer formats was a previously reported inhibitor of ITK (NCGC00188382; inhibitor #1; Fig. 2A). In extended studies, this agent demonstrated strong activity versus several cancer lines cultured in both formats (Fig. 2B). The activity of inhibitor #1 extends to a larger panel of pancreatic cancer cell lines with a heterogeneous genetic background (Fig. 2C). To cover early and late-stage phenotypes of pancreas cancer, the PANC1 and KLM-1 pancreas cancer cell models were chosen for future studies. Effective induction of apoptosis was confirmed by measure of externalization of phosphatidylserine in apoptotic cells using Annexin V after treatment for 72 hours compared with vehicle-treated PANC1 and KLM-1 spheroid cells (Fig. 2D; Supplementary Fig. S3). Treatment with inhibitor #1 effectively blocked migration and invasion of PANC1 spheroids (Fig. 2E).

Inhibitor #1 blocks metastases formation from 3D spheroid cells

Next, we examined the antimetastasis activity of inhibitor #1. PANC1 spheroid cells stably transfected with the luciferase-tagged vector pGL4.PO[luc2] were injected into the tail of pancreata of NSG mice (Supplementary Fig. S4A). Mice were treated starting on day 28 after injection with vehicle or 10 mg/kg of inhibitor #1 administered i.p. for 6 weeks when animals were harvested. Metastatic burden measured by xenogene bioluminescence and conventional histopathology was significantly reduced in animals treated with inhibitor #1 (Fig. 3A and B; Supplementary Fig. S4B and S4C). Similar findings were obtained when assessing the

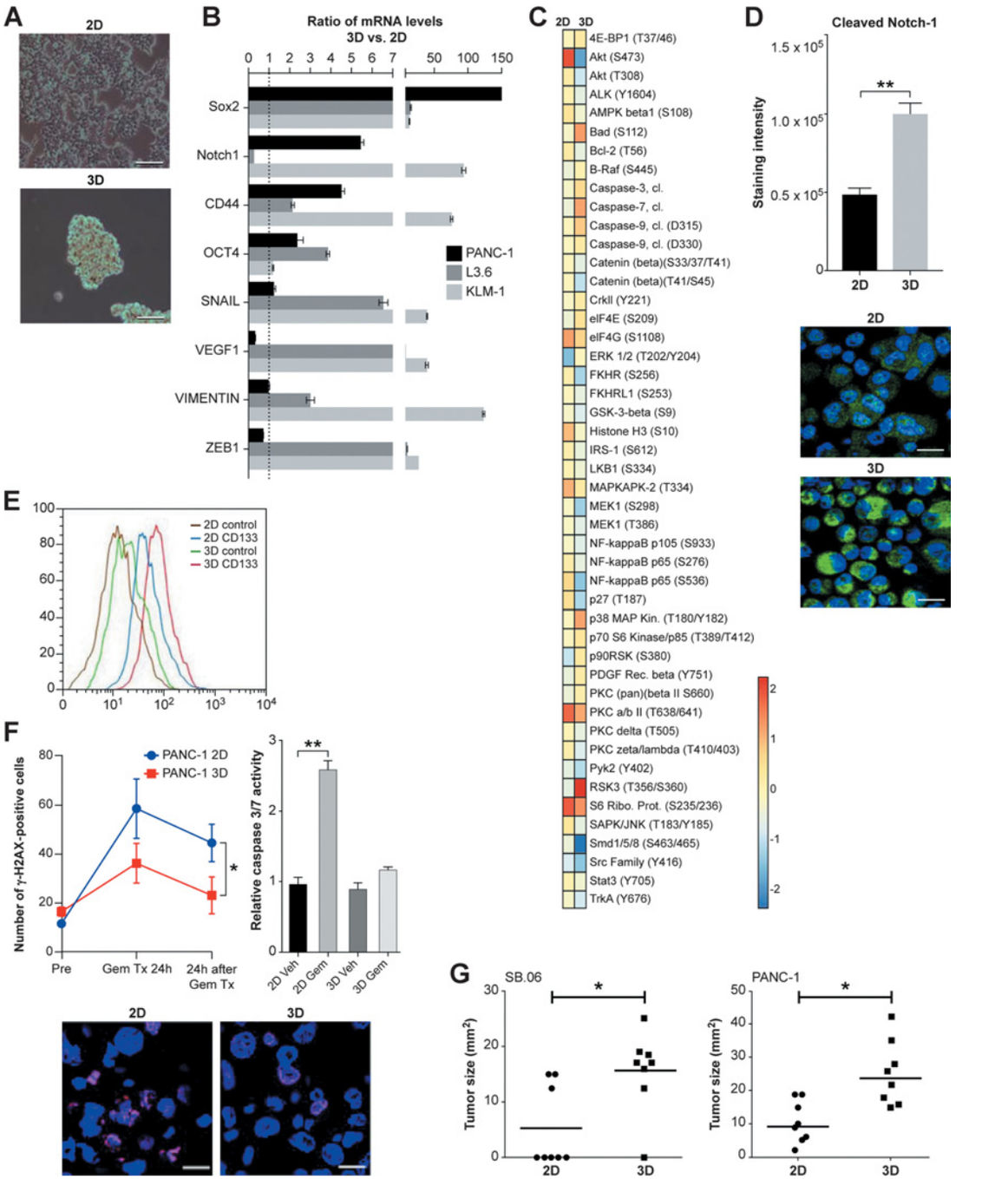

Figure 1.

Organotypic 3D spheroids harbor enriched traits of CSCs. **A,** Light microscopy of PANC1 cells grown as 2D monolayer (left) and 3D spheroids (right; 40× magnification, scale bars indicate 20 μm). **B,** Gene expression measured by qRT-PCR in cell lines PANC1, L3.6pl, and KLM-1; bars plot ratio of mean CSC gene expression levels in cells grown as spheroids vs. monolayer. Expression level in monolayer cells was set to 1 and used as a reference to calculate the fold difference in spheroids (in triplicates; $N = 5$ independent experiments; error bars, SEM). **C,** Phosphoproteomic profiling of PANC1 spheroids vs. monolayer cells. Heat map derived from RPMA, and color scale shows log-transformed values normalized to total protein. **D,** Immunofluorescence staining with anti-cleaved NOTCH1. Bar graph depicts mean intensity of 100 examined PANC1 cells (in triplicates; $N = 3$ experiments), representative images shown on bottom (scale bars, 5 μm). **E,** Histograms of PANC1 cells grown as spheroids (red) and adherent monolayer cells (blue) stained with PE-conjugated mouse monoclonal antibody against human CD133 and normalized to histogram respective isotype controls (green; brown). **F,** Immunofluorescence staining of γ-H2AX in PANC1 spheroids and monolayer cells treated with 3 μmol/L gemcitabine for 24 hours, and 24 hours after discontinuation of gemcitabine (100 cells examined, $N = 3$ independent experiments). Representative images of γ-H2AX–positive nuclei shown on bottom, caspase 3/7 levels of PANC1 monolayer cells and spheroids after treatment with 3 μmol/L gemcitabine for 72 hours shown on right (levels set to 1 of vehicle-treated control). **G,** Tumor growth 8 weeks after s.c. injection of primary low-passage patient-derived SB.06 (left) and PANC1 (right) monolayer (2D) and spheroid cells (3D) into female nu/nu mice.

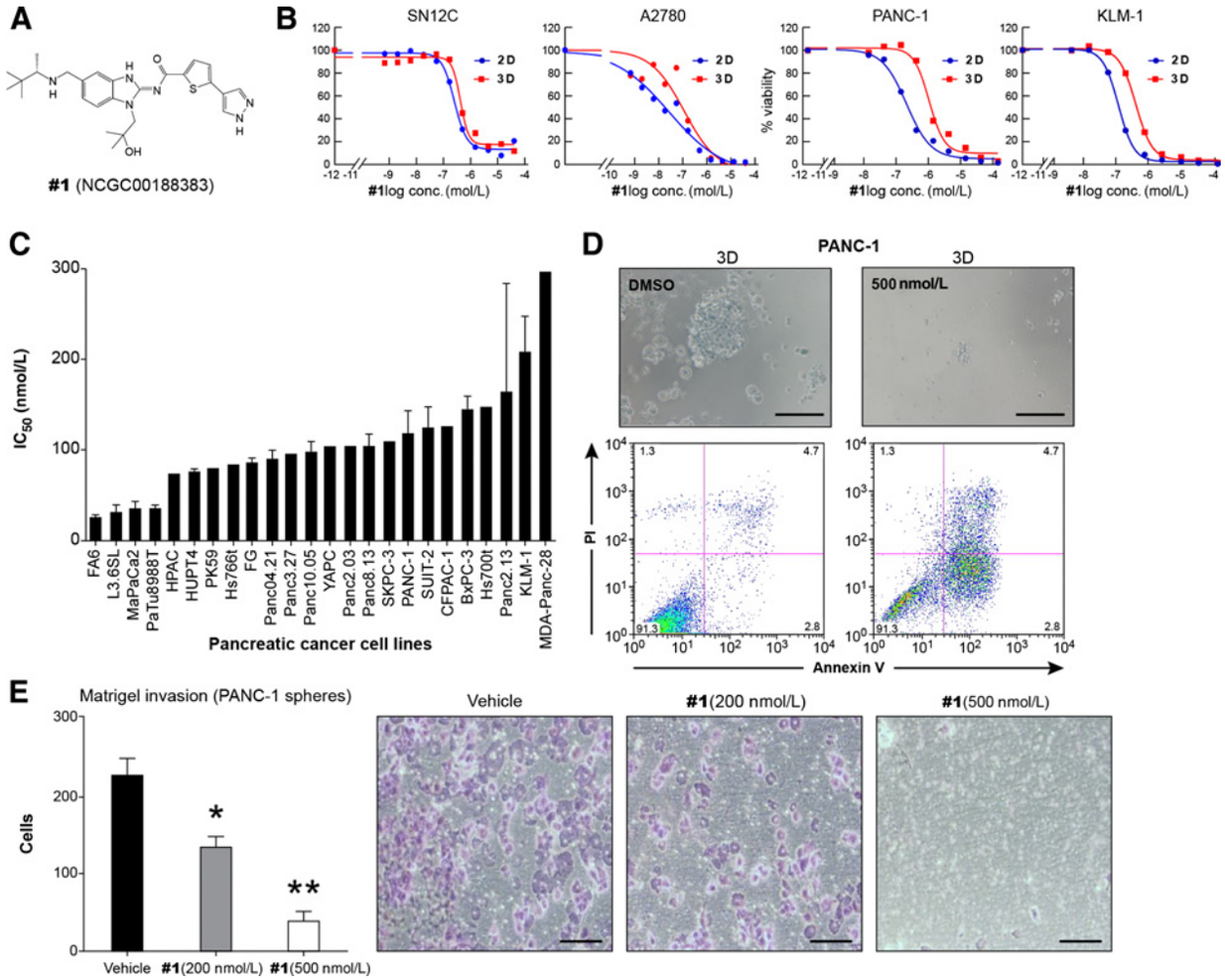

Figure 2.

Cell-based screening of PANC1 organotypic and adherent monolayer cells identifies inducible ITK inhibitor #1. **A,** Molecular structure of inhibitor #1. **B,** Complete response curves (CRC) for compound #1 in matched cell lines SN12C, A2780, PANC1, and KLM-1 [▬ monolayer (2D) cultures; ▬ spheroid (3D) cultures]. **C,** IC_{50} values (in nmol/L) in 24 pancreatic cancer cell lines following 72 hours of treatment with inhibitor #1. Bars depict the mean and SDs of three independent 10-concentration drug-response testing. **D,** Inhibitor #1 induces apoptosis in PANC1 spheroids. Flow cytometry of Annexin V–FITC (in PI stained cells; *y* axis). Spheroids were dissociated, reseeded under stem cell conditions, and treatment with inhibitor #1 was started on day 3. Cells were harvested after 72 hours, and representative images at 40× magnification are shown on top, and flow cytometry histograms on bottom. **E,** Inhibitor #1 inhibits invasion of PANC1 spheroids. Representative Diff Quick stains of PANC1 cells which transversed Matrigel-coated membranes after 18 hours. $N = 3$ independent experiments in triplicates; error bars, SEM (scale bars, 20 μm).

ability of inhibitor #1 to suppress tumor initiation. Treating NSG mice s.c. injected with 250,000 luciferase-tagged PANC1 cells with 1 and 10 mg/kg inhibitor #1 showed that the 10 mg/kg regimen significantly reduced tumor growth (Supplementary Fig. S4D). Recording fraction of percent-positive cells for cleaved NOTCH1 receptor expression in metastatic lesions, inhibitor #1-treated lesions showed reduced cleaved NOTCH1 expression levels in metastatic deposits (Fig. 3C).

In vitro and *in situ* kinome profiling identifies inhibitor #1 as a multikinase inhibitor with a distinct polypharmacological profile

To elucidate the mechanism of action of inhibitor #1, we deconvoluted potential target(s) of inhibitor #1 by first profiling the compound against a panel of over 400 kinases (DiscoveRx's KinomeScan). The outcomes from this study highlighted low nmol/L and sub-nmol/L activity versus several targets including ITK, IRAK1, IRAK4, FLT3, TAOK, and TRKC (Fig 4A; Supplementary Tables S3 and S4). As the activity of any drug is dependent upon *in situ* target engagement, inhibitor #1 was profiled next in a cell-based *in situ* kinase screen in PANC1 cells (KiNativ profile; ref. 31). MS-kinomic profiles of ATP and ADP probes allow comparative assessment of labeled kinases between treated and untreated cells. Kinases engaged by inhibitor #1 (≥50% reduction of native acyl phosphate-tagged kinases in presence of inhibitor #1; Supplementary Table S4) focused our attention on CLK1/2, EPHB2, IRAK1, AURKB, and the TAO kinases. To gain additional insight into identified targets, we examined the impact of loss of the top 8 hits from the KiNativ screen on spheroid cell survival (Fig. 4B). Loss of the MAPKK kinase thousand-and-one amino

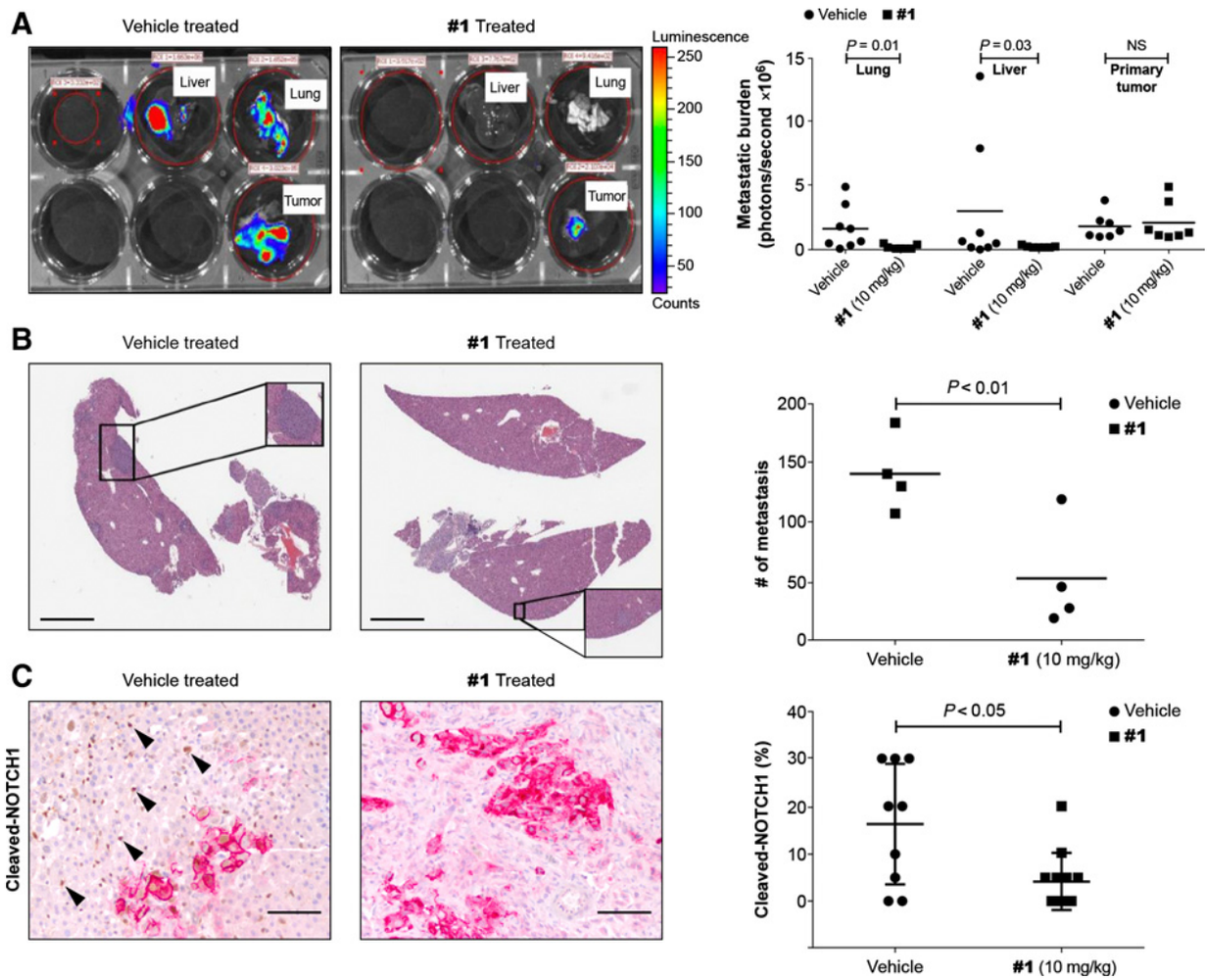

Figure 3.

Inhibitor #1 inhibits metastasis formation *in vivo*. **A,** Real-time monitoring of impact of inhibitor #1 on PANC1/*uc2* spheroid progression in orthotopic pancreatic cancer metastasis model. Tumor burden in excised distal organs in relation to primary pancreatic tumor quantified by bioluminescence imaging. Color bar indicates the intensity of the luminescent signal, with red and blue serving as the high and low signals (captured in triplicate determinations and presented as mean for each animal; $N \geq 8$ per group, representative images of excised organs are shown). **B,** Liver metastasis counted on H&E stains for both vehicle- and inhibitor #1-treated animals (right). Representative H&E stains of liver sections treated with vehicle and inhibitor #1 shown on left (scale bars, 100 μm). **C,** Inhibitor #1 decreases cleaved NOTCH1 expression in liver metastasis of treated NOD/IL2 gamma (null) PANC1 mice. Coimmunohistochemical staining of vehicle- and inhibitor #1-treated liver lesions (margins to uninvolved liver parenchyma indicated by black line) with E-Cadherin (red chromophore) and cleaved NOTCH1 (visualized by brown chromophore). Percent positive cells within metastasis shown on right.

acids protein kinase isoform 3 (TAOK3), cyclin-dependent kinase 7 (CDK7), the ephrin receptor kinase B2 (EPHB2), and aurora B kinase (AURKB) affected spheroid growth most significantly with TAOK3 producing the most profound effect compared with the other targets (Fig. 4B). Equal knockdown of target genes was confirmed by RT-PCR (Supplementary Fig. S5A). Next, we endeavored to confirm TAOK3 engagement by inhibitor #1 to accurately make mechanistic connections. Immunoprecipitated TAOK3 from pancreatic cancer cells treated with inhibitor #1 showed reduced tyrosine phosphorylation levels compared with vehicle-treated control (Fig. 4C). TAOK3 is a DNA repair kinase involved in ATM-mediated p38 activation. TAOK3-governed MKK3/6 phosphorylation and p38 activation was decreased upon treatment with inhibitor #1 in UV-treated PANC1 cells compared with vehicle-treated control (Fig. 4D; Supplementary Fig. S5B). As suggested by reduced AURKB and EPHB2 phospho levels observed in the *in situ* kinome profiling in the presence of inhibitor #1, treatment with inhibitor #1 induced a G_2–M cell-cycle arrest normally seen with inhibition of cytokinesis by aurora kinase inhibitors (Fig. 4E). In addition, phosphorylation levels of the aurora-kinase–specific phosphorylation site serine 10 on histone H3 and phosphorylation levels of the EPHB2 receptor were suppressed (Supplementary Fig. S5C and S5D). To quantify the anticancer activity of the individual targets in the context of the multikinase profile, we measured induction of apoptosis after 24 hours after silencing of one or multiple targets. The most pronounced effect as judged by Annexin V staining followed silencing of TAOK3 key combinations suggesting at least additive effects of target engagements by inhibitor #1 (Fig. 4F). The cooperating engagements of the targets TAOK3, AURKB, and

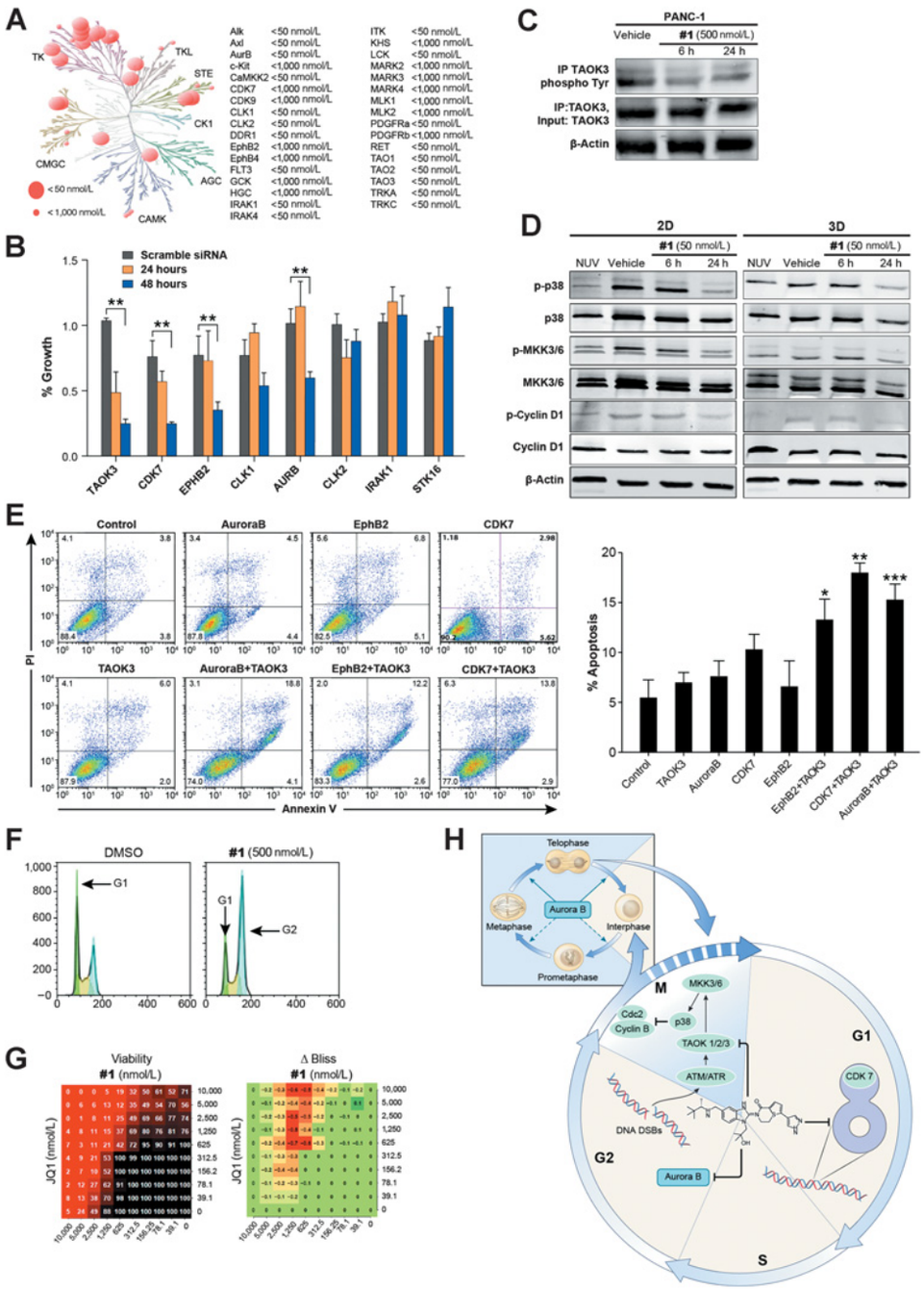

Figure 4.

Kinome profiling identifies inhibitor #1 as a multikinase inhibitor with a distinct polypharmacological profile. **A,** Dendrogram of activity profile of inhibitor #1 derived from *in vitro* kinome profiling. **B,** Impact of siRNA knockdown of targets of inhibitor #1 derived from *in situ* kinome screen onto PANC1 spheroid growth (in triplicates, error bars indicate SEMs of $N = 3$ independent experiments). **C,** Inhibitor #1 affects phosphorylation of TAOK3. TAOK3 was immunoprecipitated with anti-TAOK3 antibodies and immunoblotted with anti-phospho Tyr and anti-TAOK3. **D,** TAOK3-governed MKK3/6 phosphorylation and p38 MAPK activity decrease upon treatment with inhibitor #1. Immunoblots of PANC1 2D monolayer cells and 3D spheroids. Before cell lysis, dishes were exposed to 8 J/m^2 of UV radiation for 10 minutes, non-UV-treated (NUV) control shown on the left. **E,** Additivity in induction of apoptosis after siRNA knockdown of target combinations of #1 in PANC1 spheroids. Representative flow cytometry dot plots for Annexin V and PI of PANC1 3D spheroids treated with scramble siRNA (control), indicated target gene siRNAs, and siRNA combinations. Cells were labeled 24 hours after transfection with siRNA (bar graphs depict summary of $N = 2$ experiment, in triplicates). **F,** PI flow cytometric analysis of cell cycle. Histograms present cell-cycle distribution in PANC1 cells after 12-hour treatment with vehicle (DMSO) and inhibitor #1. **G,** Inhibitor #1 exhibits pharmacological synergy with the BET bromodomain (BET) inhibitor JQ1 as judged by 10 × 10 matrix screening in PANC1 spheroid cells. Both viability (left) and ΔBliss plots (right) are shown. **H,** Model high lightning multitier interference in DDR and cell-cycle checkpoint control by inhibitor #1.

CDK7 by inhibitor #1 involving DDR and maintenance of genome integrity, a known vulnerability of CSCs, suggest that interference with DDR mechanisms might be the driver of inhibitor #1's activity in spheroid cultures.

Next, we subjected PANC1 spheroids to unbiased small-molecule combination (matrix) screening as previously described by our group (33). Often, drug pairs displaying strong synergy, or antagonism, offer windows of insight into mechanistic pathways that contribute to the phenotypically relevant targets of a small molecule. A profile of inhibitor #1 screened in combination with a library of 463 approved and investigational drugs in discovery 6×6 matrix format provided leads that were expanded into more detailed 10×10 matrix evaluations (Supplementary Table S5; publicly available at https://tripod.nih.gov/matrix-client/). Multiple synergistic pairings were found and confirmed including combinations with actinomycin D, the HSP90 inhibitors alvespimycin (17-DMAG) and AUY922, and the proteasome inhibitor carfilzomib (Supplementary Figs. S6 and S7). The combination of inhibitor #1 with the BET BRD4 inhibitor JQ1 emerged as the top synergistic combination (Fig. 4G) which further validated the concept that inhibitor #1 disrupts cellular DDR-sensitizing PANC1 spheroids to genotoxic agents or agents increasing cellular stress (Fig. 4H).

Loss of DDR proficiency is preferentially lethal in cancer spheroids

Next, to examine whether the multitier anti-DDR function of inhibitor #1 preferentially affects tumor spheroids versus monolayer cells, we conducted a series of experiments exploring the potentiation of the genotoxic actions of gemcitabine. Alone, inhibitor #1 does not increase DNA double-strand break points as measured by induction of γ-H2AX–positive foci (Fig. 5A). However, addition of inhibitor #1 to PANC1 spheroids and monolayer cells treated with nonlethal doses of gemcitabine elicited significantly more γ-H2AX–positive foci in cells cultured as spheroids relative to monolayer cells (Fig. 5B). To examine whether TAOK3 is involved in the increased dependency of spheroids on effective DDR, we repeated the above experiment after knockdown of TAOK3. Like treatment with inhibitor #1, gemcitabine-induced DNA damage and caspase levels were increased after TAOK3 knockdown in PANC1 and KLM-1 3D spheroids compared with 2D monolayer cells (Fig. 5C; Supplementary Fig. S8A). Similarly, knockdown of the upstream DNA damage sensors ATM and ATR after gemcitabine-induced DNA damage showed reduced DDR and increased apoptosis activation in the 3D spheroids compared with the 2D monolayer cells (Fig. 5D and E; Supplementary Fig. S8B and S8C). Reduced DDR in PANC1 spheroids was also observed when DNA breaks were measured via labeling with 5-bromo-2′-deoxyuridine 5′-triphosphate (Supplementary Fig. S8D). Based upon these studies, the interference with DDR via loss of TAOK3 or other p38 pathway components, or via treatment with inhibitor #1, appears to pose a significant greater challenge to pancreatic cancer spheroids than to monolayer cells.

TAOK3 enhances pancreatic cancer stemness traits

The reduced capability of spheroids to compensate for interference with DDR mechanisms suggests a link between DDR competency and stemness. We thus investigated whether TAOK3, one of the key targets of inhibitor #1, is involved in stemness traits in pancreatic cancer next. Expression of TAOK3 was increased in spheroids versus monolayer PANC1 cells (Fig. 6A) and in tumors of surgically removed pancreatic cancers compared with matched normal pancreas of the same patient (Fig. 6B). Enforced expression of TAOK3 induced stemness mediators SOX2, NANOG, and CD44 as well as increased colony formation on soft agar (Fig. 6C and D). Injection of 1,000 KLM-1 cells transfected with TAOK3 into the flank of immunocompromised female nu/nu mice generated more and larger tumors compared with empty vector–transfected cells (Fig. 6E). Further, injection of 60,000 spheroids transfected with TAOK3 into the pancreata of NSG mice demonstrated an increased liver metastasis burden relative to cells transfected with empty vector control (Fig. 6F). Based upon these outcomes, TAOK3 promotes cancer stem–like traits of pancreas cancer cells.

Loss of TAOK3 function and treatment with #1 reduce stemness phenotypes

We next tested whether loss of TAOK3 reduces stemness traits. Silencing of TAOK3 reduced transcript levels of the stemness genes NANOG and CD44 in PANC1 spheroids and reduced anchorage-independent growth measured by colony formation on soft agar (Fig. 7A and B). Similarly, 24-hour treatment of nonlethal doses of inhibitor #1 reduced colony formation in both spheroids and monolayer cells, whereas treatment with gemcitabine had no impact on colony formation (Fig. 7C; Supplementary Fig. S8E). In line with reduced anchorage-independent growth, 24 hours of treatment with inhibitor #1 reduced transcript levels of different stemness genes, whereas gemcitabine produced no effect, or in the case of CD133 and NOTCH, increased expression levels (Fig. 7D). Furthermore, the stemness markers cleaved-NOTCH1 and CD44 cell surface expression on PANC1 spheroids decreased after 24 hours of treatment with inhibitor #1 (Fig. 7E and F). In summary, TAOK3 governs the capability of CSC-like spheroids to cope with loss of DDR function, genotoxic stress, and may provide a novel link between DDR and the CSC-like phenotype.

Discussion

Drug development in pancreatic cancer has lacked advances seen in other solid organ cancers. Self-renewing CSCs undergoing asymmetric division within their niche are able to drive pancreatic cancer progression and mediate resistance to chemo-, molecular, and radiotherapy (7, 21, 34). The presence of these progenitor-like cells correlates with poor clinical outcomes of survival and tumor recurrence (23, 35, 36). In an attempt to address these challenges, we examined how spheroid culture models responded to drug treatments relative to traditional monolayer cultures. Submitting the PANC1 cell line to HTS-enabled drug screening in both spheroid and monolayer formats provided a relative assessment of drugs with preferential or equal cell-killing phenotype in both formats (20, 27). A limited number of approved or investigational drugs demonstrated similar capacities to kill pancreatic cancer spheroids relative to monolayer cultures. Among those was a previously reported inhibitor of ITK (NCGC00188382; inhibitor #1; ref. 28). Upon profiling in multiple formats, this agent was noted to possess a complex polypharmacology with the ability to inhibit multiple targets *in situ*. Three of the four top targets (TAOK3, CDK7, and AURKB) are involved in DDR and cell-cycle checkpoint control which are mechanisms selectively upregulated and essential for survival and

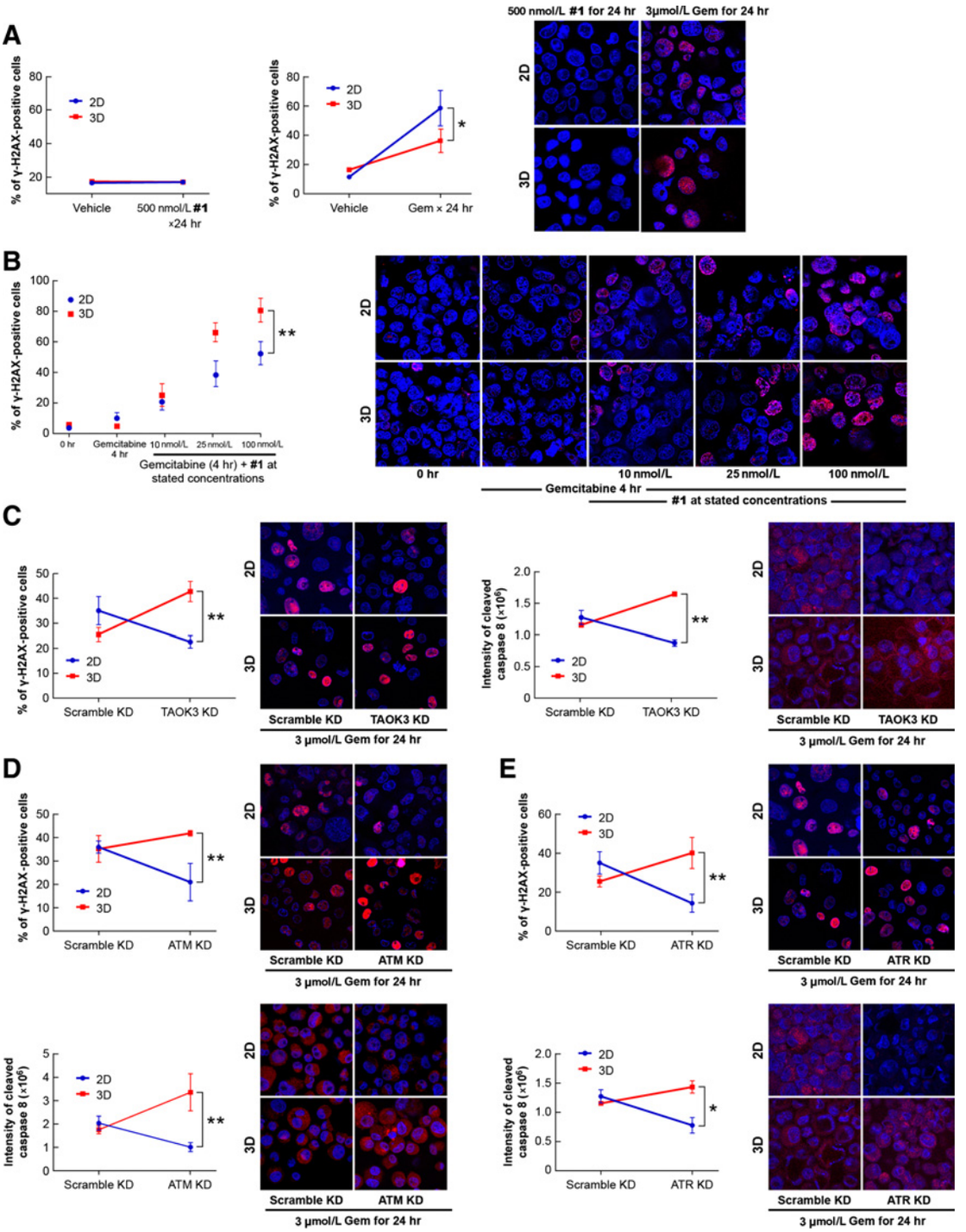

Figure 5.

PANC1 spheroids have lower capabilities to compensate for interference with DDR. **A,** γ-H2AX formation after 24 hours of treatment with inhibitor #1 (left) and 3 μmol/L gemcitabine (right) in PANC1 spheroids (red color) and monolayer cells (blue). Graph indicates mean number of γ-H2AX–positive cells of 100 examined cells; $N = 3$ independent experiments. Representative immunofluorescence images on right; scale bars, 5 μm. **B,** DNA damage in PANC1 spheroids (red) and 2D monolayer cells (blue) treated for 4 hours with 3 μmol/L of gemcitabine (gemcitabine withdrawn after 4 hours) followed by treatment of inhibitor #1 for 24 hours at indicated concentrations. **C,** Induction of γ-H2AX (left) and cleaved caspase 8 levels (right) in PANC1 spheroids (red) compared with monolayer cells (blue) treated with 3 μmol/L gemcitabine for 24 hours after transfection with scramble siRNA or TAOK3 siRNA for 48 hours (mean of 100 examined cells of $N = 3$ experiments, representative immunofluorescence images are shown). Impact of loss of (**D**) ATM and (**E**) ATR on γ-H2AX and cleaved caspase 8 levels after treatment with gemcitabine in PANC1 spheroids vs. 2D monolayer cells.

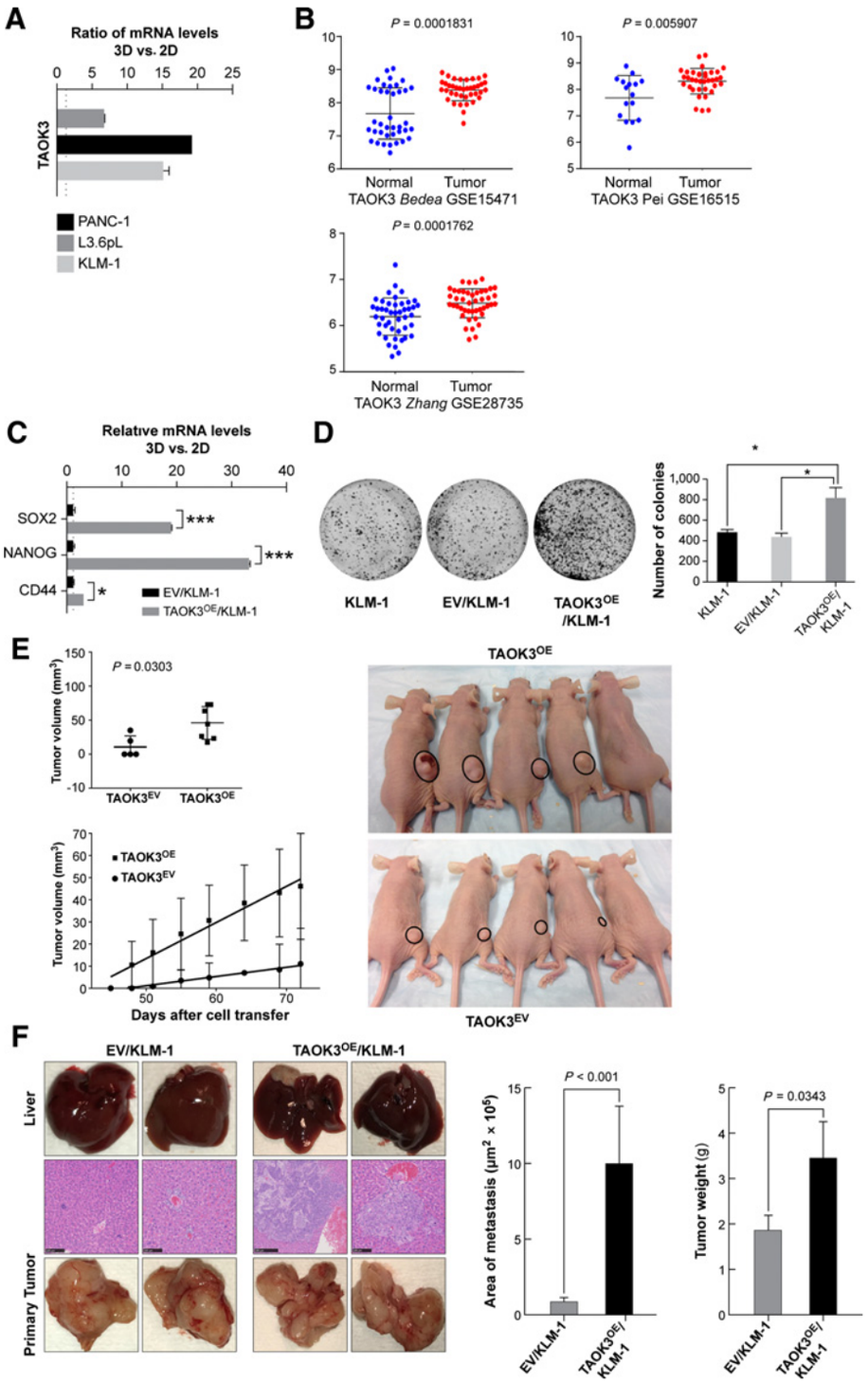

Figure 6.
Elevated TAOK3 expression is a feature of pancreatic cancer cells displaying CSC signatures. **A,** TAOK3 gene expression measured by qRT-PCR in cell lines PANC1, L3.6pl, and KLM-1. Expression levels in monolayer cells were set to #1 and used as a reference to calculate the fold difference in spheroids (in triplicates; $N = 5$). **B,** Overexpression of TAOK3 transcripts in pancreatic cancer clinical specimens compared with matched uninvolved normal pancreas (derived from gene sets GSE15471, GSE16515, and GSE28735). **C,** Enforced expression of TAOK3 increases expression levels of stemness genes SOX2, NANOG, and CD44. Expression levels of stemness genes in empty vector control cells were set to 1 (in triplicates, mean expression levels and SEMs of $N = 3$ independent experiments are shown, fold difference mRNA expression indicated on top). **D,** Anchorage-independent growth after 14 days of incubation on soft agar of nontransfected cells, KLM-1 cells transfected with empty vector GFP control, and with TAOK3. Representative soft-agar plates shown on top. **E,** Tumor volumes in nu/nu mice inoculated with 1,000 KLM-1 cells transfected with empty vector GFP control (EV) or overexpressing TAOK3 ($TAOK3^{OE}$) at 60 days after implantation (top), and longitudinal measurements shown on bottom. Representative images of animals on right, tumors indicated by black cycle. **F,** TAOK3 increases metastasis in NSG KLM-1 mice. Representative liver, primary tumor specimens at necropsy of animals and histopathology (H&E) of livers shown on the left. Quantification of liver metastasis (liver metastasis/mm^2 calculated as the sum of areas of individual metastasis of examined liver section) and primary tumor weights shown on right.

function of tumor initiating or CSCs (10, 37). CSCs enhance their DNA repair mechanisms in a variety of ways to protect their genome from accumulated replication errors during the prolonged period of quiescence (10, 13, 38).

RNAi silencing of the top targets of inhibitor #1 highlighted several compelling leads including the TAOK3 which has been reported to affect responses to cellular genotoxic events and mediate DNA damage–induced G_2–M checkpoint control via activation of p38 signaling (39). Loss of TAOK3 either via RNAi knockdown or treatment with inhibitor #1 affected DDR. Spheroids did hereby have in comparison with 2D monolayer cells a clearly limited reserve to cope with interference in DDR in response to genotoxic stress which was also shown after silencing of other DDR components. TAOK3 provides hereby an essential

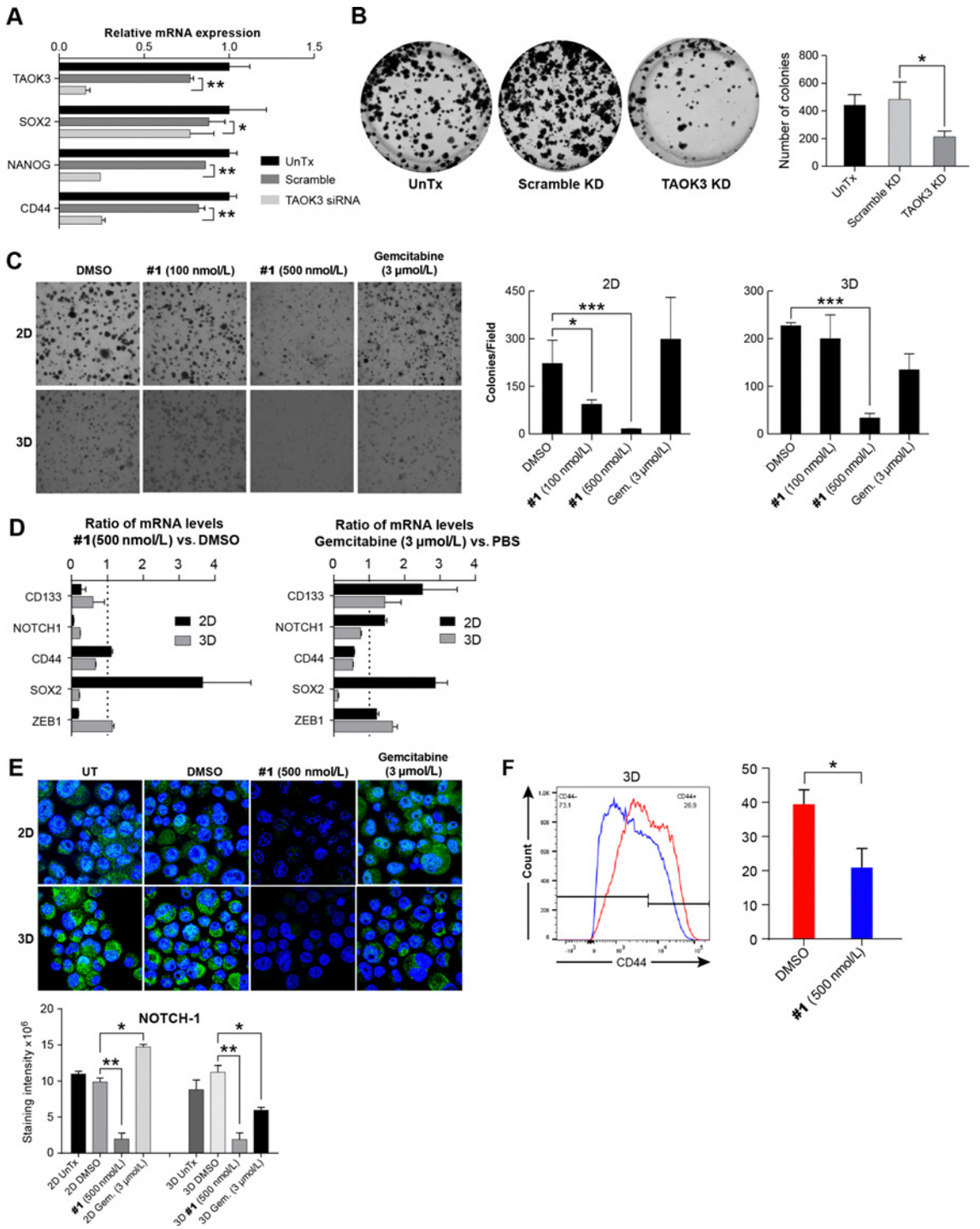

Figure 7.

Loss of TAOK3 reduces CSC traits in pancreatic cancer cells. **A,** SOX2, NANOG, and CD44 mRNA expression measured by qRT-PCR (UnTx, untreated cells; Scramble KD, scramble siRNA). **B,** TAOK3 loss decreases anchorage-independent growth. Colony formation on soft agar 14 days after transfection with scramble and anti-TAOK3 siRNA (*y* axis depicts number of colonies; $N = 3$). **C,** Treatment with inhibitor #1 reduces colony formation compared with gemcitabine. Number of colonies of PANC1 monolayer cells and spheroids after treatment with 100 nmol/L and 500 nmol/L inhibitor #1 or 3 μmol/L gemcitabine. Colony numbers after 14 days are depicted on *y* axis. **D,** Expression levels of stemness genes measured by qRT-PCR after 24 hours of treatment with inhibitor #1 and gemcitabine compared with vehicle-treated values in both PANC1 monolayer cells and spheroids. **E,** Inhibitor #1 reduces cleaved NOTCH1 levels in PANC1 cells. Quantitative immunofluorescence of PANC1 2D monolayer cells (representative images, top row) and spheroids (bottom) treated for 24 hours with 500 nmol/L inhibitor #1 or 3 μmol/L gemcitabine. Quantification of mean fluorescence intensity (100 cells examined, $N = 2$ independent experiments, in triplicates) on bottom. **F,** Inhibitor #1 reduces CD44 expression on PANC1 spheroids. Flow cytometry histogram of vehicle (blue) and inhibitor #1-treated (red) PANC1 spheroids.

link between DDR competency and stemness. TAOK3 was noted to be upregulated in pancreatic spheroid models and forced expression of TAOK3 increased the expression of SOX2, NANOG, and CD44. Overexpression of TAOK3 increased colony formation and *in vivo* tumor initiation and metastatic burden. Conversely, knockdown of TAOK3 had a negative influence on stemness traits. Previous reports connecting DDR competency and cancer stemness–like phenotype included ATM which was shown to be a checkpoint for self-renewal in melanocytes, p38 MAPK negatively regulating stemness phenotypes in NSCLC, aurora kinase promoting metastasis via the acquisition of stem cell–like properties and epithelial-mesenchymal transition (EMT), or RAD6 promoting stemness and DDR in ovarian cancer (40–43). Thus, there is intense interest in the development of DDR inhibitors like CHK, PARP, or p38 inhibitors in combination with cytotoxic chemotherapy to overcome the challenges of drug resistance mediated by CSCs (44, 45). In this regard, a first-in-human early clinical signal of targeting TAOK3-related signaling was just released. Using the small-molecule ATR inhibitor M6620, with ATR being directly upstream of TAOK3, in combination with topotecan, M6620 showed within a phase I study early clinical activity in solid organ cancers heavily pretreated with cytotoxic chemotherapy (46). It has to be seen if currently employed agents targeting CHK1, CHK2, WEE1, or DNA-PK in combination with current standard-of-care therapies are the best anti-CSC option (45). In this regard, the synergistic combinations derived from matrix screening of spheroids in this study provide novel leads for addressing tumor heterogeneity. For example, the strong cooperativity of DDR and proteasome inhibitors seem to suggest yet unexplored options targeting the CSC-like phenotype.

The presented study is not without limitations. Although TAOK3 promotes metastasis, we cannot define how much of the antimetastasis effect of inhibitor #1 in the NSG PANC1 mice is due to inhibitor #1's anti-TAOK3 effect. It is possible that the previously described antimetastasis mechanism of action of aurora kinase inhibitors is predominantly driving this phenotype (41). Although the combination of *in vitro* RNAi studies in 3D spheroids suggests cooperativity between the individual targets of inhibitor #1, their individual impact might be different *in vivo* (47, 48).

In summary, based upon these studies, TAOK3 appears to be a novel anti-CSC target as it mediates CSC traits including tumor initiation and metastasis formation. The increased dependency of tumor spheroids on TAOK3 and DDR function may yield a novel mean for the selective reduction, or eradication, of CSC populations.

Disclosure of Potential Conflicts of Interest

No potential conflicts of interest were disclosed.

Authors' Contributions

Conception and design: Y. Bian, Y. Teper, L.A. Mathews Griner, M. Ferrer, C.J. Thomas, U. Rudloff

Development of methodology: Y. Bian, Y. Teper, L.A. Mathews Griner, P. Shinn, H.-W. Xin, D. Li, M. Ferrer, C.J. Thomas, U. Rudloff

Acquisition of data (provided animals, acquired and managed patients, provided facilities, etc.): Y. Bian, Y. Teper, L.A. Mathews Griner, T.J. Aiken, V. Shukla, H.-W. Xin, H. Pflicke, A.S. Powers, P. Patel, C.J. Thomas, U. Rudloff

Analysis and interpretation of data (e.g., statistical analysis, biostatistics, computational analysis): Y. Bian, Y. Teper, L.A. Mathews Griner, T.J. Aiken, V. Shukla, R. Guha, H.-W. Xin, P. Patel, M. Ferrer, C.J. Thomas, U. Rudloff

Writing, review, and/or revision of the manuscript: Y. Bian, Y. Teper, L.A. Mathews Griner, R. Guha, M. Ferrer, C.J. Thomas, U. Rudloff

Administrative, technical, or material support (i.e., reporting or organizing data, constructing databases): Y. Bian, Y. Teper, P. Shinn, D. Li, J.-k. Jiang, J. Aubé, C.J. Thomas

Study supervision: Y. Bian, M. Ferrer, C.J. Thomas, U. Rudloff

Acknowledgments

This research was supported by the Intramural Research Program of the National Institutes of Health, National Cancer Institute (ZIA BC 011267). The content of this publication does not reflect the views of policies of the Department of Health and Human Services, nor does mention of trade names, commercial products, or organizations imply endorsement by the U.S. government. We thank Alan Hoofring from Medical Illustration, NIH Medical Arts Branch, for his significant help with the figure development for this article.

The costs of publication of this article were defrayed in part by the payment of page charges. This article must therefore be hereby marked *advertisement* in accordance with 18 U.S.C. Section 1734 solely to indicate this fact.

Received September 6, 2018; revised March 11, 2019; accepted July 29, 2019; published first August 8, 2019.

References

1. Siegel RL, Miller KD, Jemal A. Cancer statistics, 2016. CA Cancer J Clin 2016;66:7–30.
2. Rahib L, Smith BD, Aizenberg R, Rosenzweig AB, Fleshman JM, Matrisian LM. Projecting cancer incidence and deaths to 2030: the unexpected burden of thyroid, liver, and pancreas cancers in the United States. Cancer Res 2014;74:2913–21.
3. Ma J, Jemal A.The rise and fall of cancer mortality in the USA: why does pancreatic cancer not follow the trend? Future Oncol 2013;9:917–9.
4. Conroy T, Desseigne F, Ychou M, Bouché O, Guimbaud R, Bécouarn Y, et al. FOLFIRINOX versus gemcitabine for metastatic pancreatic cancer. N Engl J Med 2011;364:1817–25.
5. Von Hoff DD, Ervin T, Arena FP, Chiorean EG, Infante J, Moore M, et al. Increased survival in pancreatic cancer with nab-paclitaxel plus gemcitabine. N Engl J Med 2013;369:1691–703.
6. Hermann PC, Huber SL, Herrler T, Aicher A, Ellwart JW, Guba M, et al. Distinct populations of cancer stem cells determine tumor growth and metastatic activity in human pancreatic cancer. Cell Stem Cell 2007;1: 313–23.
7. Kreso A, Dick JE.Evolution of the cancer stem cell model. Cell Stem Cell 2014;14:275–91.
8. Cabarcas SM, Mathews LA, Farrar WL. The cancer stem cell niche–there goes the neighborhood? Int J Cancer 2011;129:2315–27.
9. Plaks V, Kong N, Werb Z. The cancer stem cell niche: how essential is the niche in regulating stemness of tumor cells? Cell Stem Cell 2015;16: 225–38.
10. Vitale I, Manic G, De Maria R, Kroemer G, Galluzzi L. DNA damage in stem cells. Mol Cell 2017;66:306–19.
11. Lim YC, Roberts TL, Day BW, Harding A, Kozlov S, Kijas AW, et al. A role for homologous recombination and abnormal cell-cycle progression in radioresistance of glioma-initiating cells. Mol Cancer Ther 2012;11: 1863–72.
12. Yuan M, Eberhart CG, Kai M. RNA binding protein RBM14 promotes radioresistance in glioblastoma by regulating DNA repair and cell differentiation. Oncotarget 2014;5:2820–6.
13. Bao S, Wu Q, McLendon RE, Hao Y, Shi Q, Hjelmeland AB, et al. Glioma stem cells promote radioresistance by preferential activation of the DNA damage response. Nature 2006;444:756–60.
14. Bartucci M, Svensson S, Romania P, Dattilo R, Patrizii M, Signore M, et al. Therapeutic targeting of Chk1 in NSCLC stem cells during chemotherapy. Cell Death Differ 2012;19:768–78.

15. Beerman I, Seita J, Inlay MA, Weissman IL, Rossi DJ. Quiescent hematopoietic stem cells accumulate DNA damage during aging that is repaired upon entry into cell cycle. Cell Stem Cell 2014;15:37–50.
16. Ito K, Suda T.Metabolic requirements for the maintenance of self-renewing stem cells. Nat Rev Mol Cell Biol 2014;15:243–56.
17. Mathews Griner LA, Zhang X, Guha R, McKnight C, Goldlust IS, Lal-Nag M, et al. Large-scale pharmacological profiling of 3D tumor models of cancer cells. Cell Death Dis 2016;7:e2492.
18. Broutier L, Mastrogiovanni G, Verstegen MM, Francies HE, Gavarró LM, Bradshaw CR, et al. Human primary liver cancer-derived organoid cultures for disease modeling and drug screening. Nat Med 2017;23:1424–35.
19. Li C, Heidt DG, Dalerba P, Burant CF, Zhang L, Adsay V, et al. Identification of pancreatic cancer stem cells. Cancer Res 2007;67:1030–7.
20. Jaiswal KR, Xin HW, Anderson A, Wiegand G, Kim B, Miller T, et al. Comparative testing of various pancreatic cancer stem cells results in a novel class of pancreatic-cancer-initiating cells. Stem Cell Res 2012;9: 249–60.
21. Xin HW, Ambe CM, Hari DM, Wiegand GW, Miller TC, Chen JQ, et al. Label-retaining liver cancer cells are relatively resistant to sorafenib. Gut 2013;62:1777–86.
22. Kim MP, Fleming JB, Wang H, Abbruzzese JL, Choi W, Kopetz S, et al. ALDH activity selectively defines an enhanced tumor-initiating cell population relative to CD133 expression in human pancreatic adenocarcinoma. PLoS One 2011;6:e20636.
23. Gupta PB, Onder TT, Jiang G, Tao K, Kuperwasser C, Weinberg RA, et al. Identification of selective inhibitors of cancer stem cells by high-throughput screening. Cell 2009;138:645–59.
24. Gujral TS, Peshkin L, Kirschner MW. Exploiting polypharmacology for drug target deconvolution. Proc Natl Acad Sci U S A 2014;111:5048–53.
25. Mathews Griner LA, Guha R, Shinn P, Young RM, Keller JM, Liu D, et al. High-throughput combinatorial screening identifies drugs that cooperate with ibrutinib to kill activated B-cell-like diffuse large B-cell lymphoma cells. Proc Natl Acad Sci U S A 2014;111:2349–54.
26. Paolini GV, Shapland RH, van Hoorn WP, Mason JS, Hopkins AL. Global mapping of pharmacological space. Nat Biotechnol 2006;24:805–15.
27. Hopkins AL. Network pharmacology: the next paradigm in drug discovery. Nat Chem Biol 2008;4:682–90.
28. Riether D, Zindell R, Kowalski JA, Cook BN, Bentzien J, Lombaert SD, et al. 5-Aminomethylbenzimidazoles as potent ITK antagonists. Bioorg Med Chem Lett 2009;19:1588–91.
29. Mathews LA, Cabarcas SM, Hurt EM, Zhang X, Jaffee EM, Farrar WL. Increased expression of DNA repair genes in invasive human pancreatic cancer cells. Pancreas 2011;40:730–9.
30. Mathews LA, Keller JM, Goodwin BL, Guha R, Shinn P, Mull R, et al. A 1536-well quantitative high-throughput screen to identify compounds targeting cancer stem cells. J Biomol Screen 2012;17:1231–42.
31. Patricelli MP, Nomanbhoy TK, Wu J, Brown H, Zhou D, Zhang J, et al. In situ kinase profiling reveals functionally relevant properties of native kinases. Chem Biol 2011;18:699–710.
32. Boyd ZS, Wu QJ, O'Brien C, Spoerke J, Savage H, Fielder PJ, et al. Proteomic analysis of breast cancer molecular subtypes and biomarkers of response to targeted kinase inhibitors using reverse-phase protein microarrays. Mol Cancer Ther 2008;7:3695–706.
33. Straussman R, Morikawa T, Shee K, Barzily-Rokni M, Qian ZR, Du J, et al. Tumour micro-environment elicits innate resistance to RAF inhibitors through HGF secretion. Nature 2012;487:500–4.
34. Xin HW, Hari DM, Mullinax JE, Ambe CM, Koizumi T, Ray S, et al. Tumor-initiating label-retaining cancer cells in human gastrointestinal cancers undergo asymmetric cell division. Stem Cells 2012;30:591–8.
35. Li C, Wu JJ, Hynes M, Dosch J, Sarkar B, Welling TH, et al. c-Met is a marker of pancreatic cancer stem cells and therapeutic target. Gastroenterology 2011;141:2218–27e2215.
36. Ohara Y, Oda T, Sugano M, Hashimoto S, Enomoto T, Yamada K, et al. Histological and prognostic importance of CD44(+) /CD24(+) /EpCAM (+) expression in clinical pancreatic cancer. Cancer Sci 2013;104:1127–34.
37. Mathews LA, Cabarcas SM, Farrar WL. DNA repair: the culprit for tumor-initiating cell survival? Cancer Metastasis Rev 2011;30:185–97.
38. Zhang M, Behbod F, Atkinson RL, Landis MD, Kittrell F, Edwards D, et al. Identification of tumor-initiating cells in a p53-null mouse model of breast cancer. Cancer Res 2008;68:4674–82.
39. Raman M, Earnest S, Zhang K, Zhao Y, Cobb MH. TAO kinases mediate activation of p38 in response to DNA damage. EMBO J 2007;26:2005–14.
40. Inomata K, Aoto T, Binh NT, Okamoto N, Tanimura S, Wakayama T, et al. Genotoxic stress abrogates renewal of melanocyte stem cells by triggering their differentiation. Cell 2009;137:1088–99.
41. D'Assoro AB, Liu T, Quatraro C, Amato A, Opyrchal M, Leontovich A, et al. The mitotic kinase Aurora–a promotes distant metastases by inducing epithelial-to-mesenchymal transition in ERalpha(+) breast cancer cells. Oncogene 2014;33:599–610.
42. Fang Y, Wang J, Wang G, Zhou C, Wang P, Zhao S, et al. Inactivation of p38 MAPK contributes to stem cell-like properties of non-small cell lung cancer. Oncotarget 2017;8:26702–17.
43. Somasagara RR, Spencer SM, Tripathi K, Clark DW, Mani C, Madeira da Silva L, et al. RAD6 promotes DNA repair and stem cell signaling in ovarian cancer and is a promising therapeutic target to prevent and treat acquired chemoresistance. Oncogene 2017;36:6680–90.
44. Sosa MS, Avivar-Valderas A, Bragado P, Wen HC, Aguirre-Ghiso JA. ERK1/2 and p38alpha/beta signaling in tumor cell quiescence: opportunities to control dormant residual disease. Clin Cancer Res 2011;17:5850–7.
45. Brandsma I, Fleuren EDG, Williamson CT, Lord CJ. Directing the use of DDR kinase inhibitors in cancer treatment. Expert Opin Investig Drugs 2017;26:1341–55.
46. Thomas A, Redon CE, Sciuto L, Padiernos E, Ji J, Lee MJ, et al. Phase I study of ATR inhibitor M6620 in combination with topotecan in patients with advanced solid tumors. J Clin Oncol 2018;36:1594–602.
47. Zheng X, Carstens JL, Kim J, Scheible M, Kaye J, Sugimoto H, et al. Epithelial-to-mesenchymal transition is dispensable for metastasis but induces chemoresistance in pancreatic cancer. Nature 2015;527: 525–30.
48. Atapattu L, Saha N, Chheang C, Eissman MF, Xu K, Vail ME, et al. An activated form of ADAM10 is tumor selective and regulates cancer stem-like cells and tumor growth. J Exp Med 2016;213:1741–57.